
Measurements of Core and Pusher Conditions in Surrogate Capsule Implosions on the OMEGA Laser System

The primary objective of the experimental program at LLE is to evaluate the direct-drive approach to laser-driven inertial confinement fusion (ICF). In particular, its central goal is to validate, by using the 30-kJ, 351-nm, 60-beam OMEGA laser system,¹ the performance of high-gain, direct-drive target designs planned for use on the National Ignition Facility (NIF). This will be achieved by diagnosing the implosion of cryogenic, solid-DT-shell capsules that are hydrodynamically equivalent to the ignition/high-gain capsules planned for use on the NIF with a 1- to 2-MJ drive. In the direct-drive approach to fusion, the capsule is directly irradiated by a large number of symmetrically arranged laser beams, as opposed to the indirect approach in which the driver energy is first converted into x rays, which then drive the capsule. Direct drive has the potential to be more efficient since it does not require this intermediate x-ray conversion step. In both cases the high densities and core temperatures necessary for ignition require that the capsules must be imploded with minimal departures from one-dimensional behavior. For direct-drive capsules, the dominant effect contributing to degradations in capsule performance is believed to be the development of Rayleigh–Taylor (RT) unstable growth,² seeded by either laser-irradiation non-uniformities or capsule imperfections.

In a direct-drive capsule implosion, the development of hydrodynamic instabilities occurs in a number of stages. In the start-up, or imprinting, phase the laser is directly incident on the solid capsule surface. Eventually, a plasma is created due to either dielectric breakdown or other processes, a critical surface is formed, and the absorption of laser light sends a series of shocks into the target, eventually causing the shell to move and begin to accelerate. During this initial phase, nonuniformities present in the laser will cause nonuniform shocks to be launched into the target, resulting in imposed modulations and a certain amount of unstable growth during the shock transit period due to Richtmyer–Meshkov³ (shock-driven) or RT (acceleration-driven) instability. During the subsequent acceleration phase of the implosion, RT growth continues to grow at the ablation surface with a growth rate that can be approximated by^{4,5}

$$\gamma = \alpha \sqrt{[kg(t)]} - \beta kV_a(t), \quad (1)$$

where k is the unstable wave number, $g(t)$ is the acceleration, and $V_a(t)$ is the ablation velocity. The distortions that grow at the ablation surface can eventually feed through to the inner surface of the shell, where they add to any existing mass perturbations, thus seeding an instability that can grow at that surface as the target begins to decelerate during stagnation. If the resultant distortions are large enough, the performance of the capsule will be severely compromised. An integrated understanding of hydrodynamic instabilities, fuel–pusher mix, and their effect on capsule performance requires quantitative data and a study of the processes involved in each phase.

In this article we present the results of direct-drive experiments carried out on OMEGA to investigate each of the stages described above. First, we summarize the results of experiments designed to study the imprint and acceleration stages, in both planar and spherical geometries. Next we present the first phase of the investigation of the deceleration stage. [This stage has previously been investigated in indirectly driven targets at the Lawrence Livermore National Laboratory (LLNL) using plastic targets with an inner layer of Ti-doped CH and an Ar-doped D₂ fill.^{6–8}] The goal of our initial experiments was to ensure that our diagnostics could measure the conditions in both the core and the shell during shell deceleration and stagnation and that they had enough sensitivity to observe differences in core conditions under various RT-growth conditions. The RT growth was modified by varying the temporal pulse shape (Gaussian or square) and by doping the outer 6 μm of the CH shell with chlorine.

The deceleration stage was studied by irradiating ~1-mm-diam, 20-μm-thick CH shells with 30 kJ of 351-nm, 1-ns laser pulses. No smoothing techniques were applied to the laser beams. The one-dimensional simulations of the experiments were carried out with the hydrodynamic code *LILAC*,⁹ which includes ray tracing of the laser light, *SESAME*¹⁰ equations of state, multigroup radiation transport, and non-LTE average-

ion capability. A few simulations were carried out with the two-dimensional code *ORCHID*¹¹ to investigate qualitatively the effect of the RT growth on the target during the acceleration, deceleration, and stagnation of the shell.

Imprint and Acceleration Phases

Direct measurements of laser imprinting are extremely difficult, although Kalantar *et al.*¹² have reported measurements of imprint in thin Si and Al foils using an x-ray laser as a backlighter. Measurements on OMEGA to date have relied on the technique of x-ray radiography of laser-accelerated CH foils in planar geometry,^{13–17} using a uranium backlighter with an average photon energy of ~ 1.3 keV. Modulations in the optical depth of the driven foil measured at different times by an x-ray framing camera are used to observe the growth of perturbations seeded by imprinting. However, since the initial perturbations created by the laser imprint are too small to be measured directly by this method, the optical-depth measurements are not taken until the foil has accelerated and undergone a significant amount of RT growth in order to amplify the initial perturbation to detectable levels. This measurement therefore incorporates the combined effects of the imprint phase, shock transit phase, and a portion of the acceleration phase. Despite the complication added by the RT growth, such measurements are invaluable for comparing the effects of irradiation-uniformity changes, beam-smoothing techniques, and other mitigation schemes.

Face-on radiography of foils with intentionally imposed single-mode, sinusoidal mass perturbations were used to compare calculated RT-growth rates with experimental measurements. (These experiments are a continuation of the collaboration between LLE and LLNL.¹⁴ Similar experiments have also been performed in indirect drive.¹⁸) In these measurements an x-ray streak camera or framing camera is used to measure the optical depth of the imposed mode as a function of time in much the same way as in the imprint measurements. In addition, side-on measurements of foil trajectory were used¹⁹ to confirm that coupling of laser energy into the foils was in agreement with simulations. Results from single-mode experiments carried out on OMEGA are shown in Fig. 74.37. In these plots, the optical depth of the observed modulation of the backlighter, as seen through the accelerated foil, is plotted as a function of time, together with predictions from the 2-D hydrodynamic code *ORCHID*. (A more detailed description of this data can be found in Ref. 19.) The excellent agreement between the experimental data and the simulations is strong evidence that, for polymer materials, the RT unstable growth can be calculated accurately.

In spherical target experiments, where there is no diagnostic access to the rear surface of the shell, we have inferred the development of instability growth at the ablation surface during the acceleration phase through use of the so-called “burnthrough” technique.²⁰ In this method, time-resolved

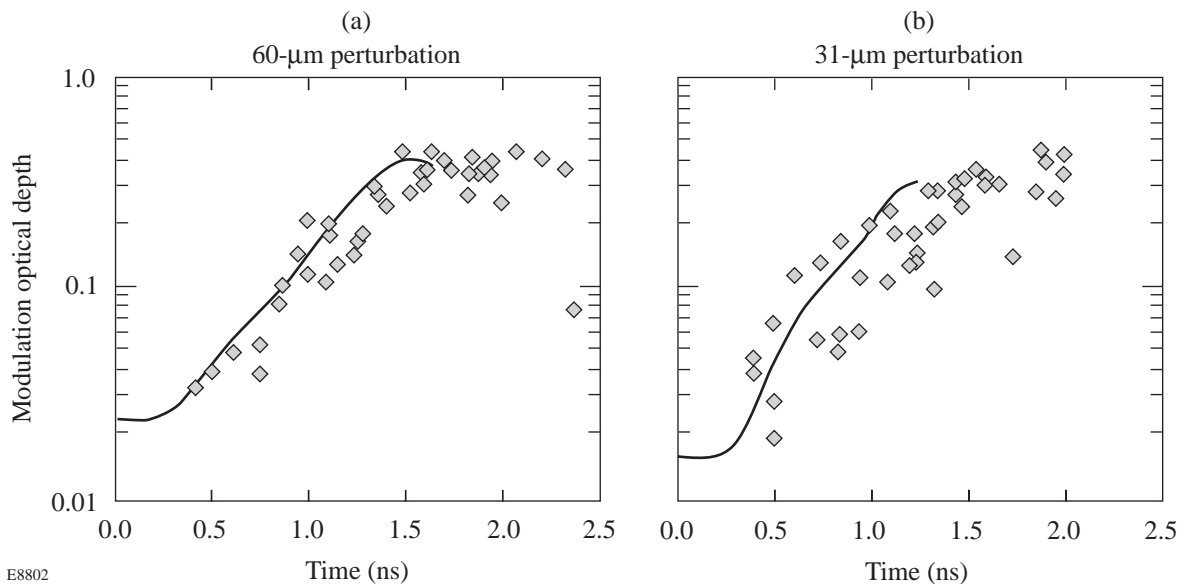


Figure 74.37
Results from the single-mode planar experiments (◆) conducted on the OMEGA laser compared to *ORCHID* simulations (solid line) for (a) 60- μm and (b) 31- μm perturbation wavelengths.

spectroscopy, using a spectrally dispersing x-ray streak camera, is used to detect the onset of x-ray emission from a buried signature layer. In the absence of any unstable growth or perturbation, the heat front propagates uniformly through the CH ablator until it reaches the signature layer and heats it, resulting in characteristic x-ray line emission. The presence of unstable growth, however, produces a mix region that can leach signature layer material out to the heat front, causing early emission. This method has been shown to be very sensitive to initial beam uniformity²¹ and to target acceleration and effective Atwood number.²⁰ As with the planar-foil imprint measurements, this method measures the combined effects of imprint coupled with RT growth.

We conducted a series of burnthrough experiments with unsmoothed laser beams to provide a baseline for subsequent uniformity improvements scheduled for the OMEGA laser system. The targets used chlorinated plastic (C_8H_7Cl) as the signature layer, with CH ablator overcoats ranging from 8 to 12 μm . The target diameters were 900 to 950 μm , and in all cases the total shell thickness was 20 μm . The capsules were overcoated with a 1000- \AA Al barrier layer to act as a timing reference mark and to prevent shinethrough²² of the early part of the laser pulse into the target before formation of the critical

surface. In these experiments, the targets were imploded by 60 beams, focused tangentially to the target, with a 1-ns full-width-at-half-maximum (FWHM) Gaussian temporal profile and a total of 20 to 25 kJ. Spectral dispersion for the x-ray streak camera was provided by a flat rubidium acid phthalate (RbAP) crystal, providing coverage of the K -shell spectrum of the Al overcoat in first-order Bragg diffraction, simultaneous with coverage of chlorine lines in second order. The data from these experiments, together with a typical streak camera image, are shown in Fig. 74.38(a). The time-resolved spectrum [Fig. 74.38(a)] shows Al lines, formed when the laser is initially incident on the outside of the capsule, and, after a delay of several hundred picoseconds, emission from the buried C_8H_7Cl layer. The measurements have been modeled using a postprocessor to *LILAC* that calculates the mix thickness using the Haan²³ method from an experimentally measured initial perturbation spectrum. (Full details of the model are given in Ref. 20.) Figure 74.38(b) shows a comparison of the experimental burnthrough times and those predicted by the model, as a function of CH ablator thickness. The two cases were normalized for one of the 9- μm cases. Variations in burnthrough time for a given ablator thickness are caused primarily by laser energy variations between shots. The burnthrough times predicted by *LILAC* for the uniform 1-D case are also shown and

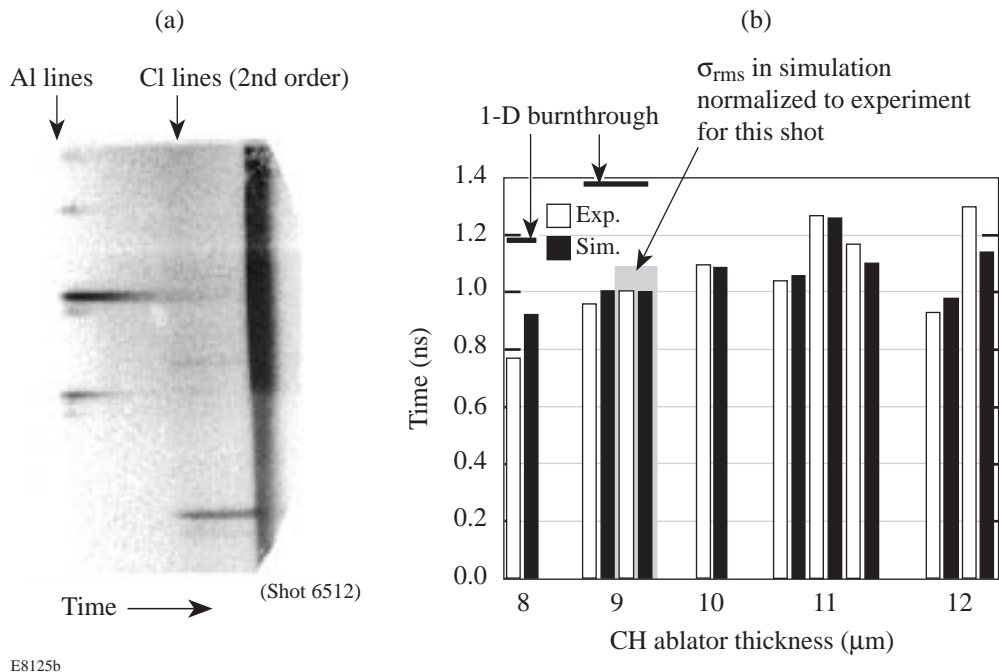


Figure 74.38

Results from burnthrough experiments carried out on the 60-beam OMEGA laser. (a) The streak camera spectrum shows the onset of the Cl lines from the Cl-doped substrate at the time of burnthrough. (b) Burnthrough times from the mix postprocessor to *LILAC* are compared to the experimental data for targets with increasing ablator thickness.

indicate that much-later-than-observed burnthrough would be expected for the 8- and 9- μm ablators, with no burnthrough expected for the thicker cases. The good agreement between the simulations and the experiment over a range of target parameters confirms our confidence in the model and shows that we are now well placed to diagnose planned improvements to laser uniformity.

Deceleration Phase

Initial measurements on deceleration-phase instability utilized a series of surrogate capsules, consisting of a CH shell filled with deuterium gas. These targets are designed to mimic the behavior of future OMEGA cryogenic DT capsules (and, by extension, NIF ignition capsules) by approximating their gross hydrodynamic behavior (e.g., similar in-flight aspect ratio and convergence). For the purposes of these experiments, the CH shell represents the main-fuel-layer region in a cryogenic ignition target, and the D_2 gas represents the fuel hot spot. Figure 74.39 shows the standard capsule we have used to investigate these two regions. The hot spot, or in our case the gas region, consists of 20 atm of D_2 , doped with 0.25% Ar as a spectroscopic signature. The shell consists of a 20- μm CH layer in which is buried a 1- μm layer of (1%–4%) Ti-doped CH. The doped layer can be positioned at various distances from the shell/ D_2 interface, allowing the study of conditions at different positions inside the shell/main fuel layer. This differs from the method described in Ref. 6, in which the Ti-doped layer was situated only at the pusher/fuel interface.

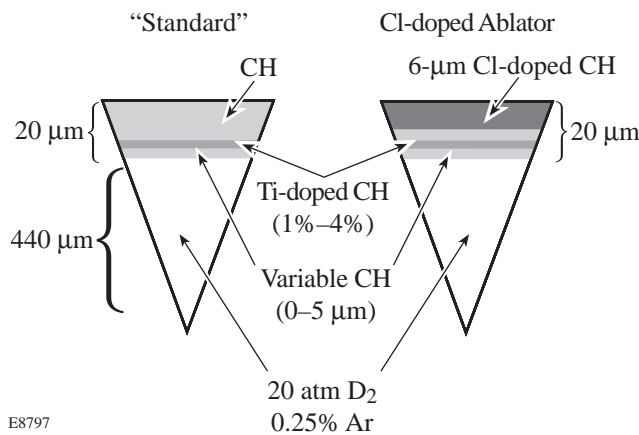


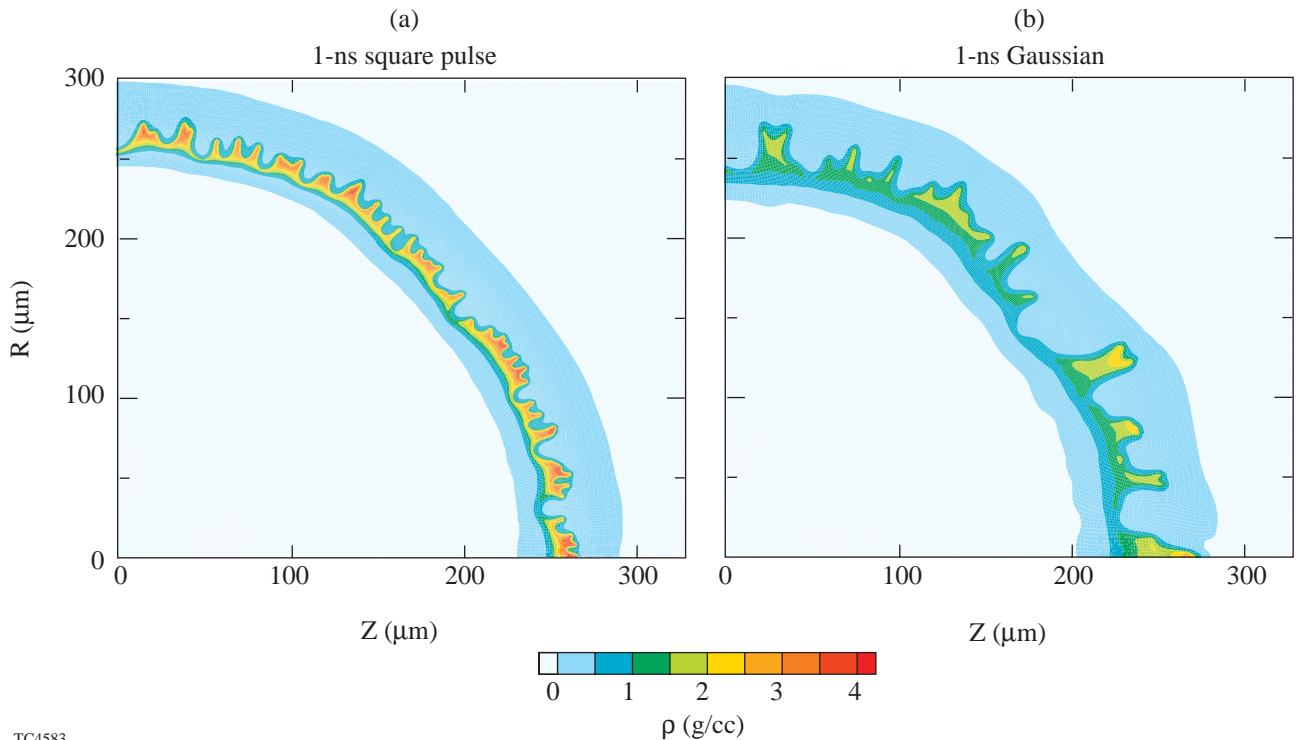
Figure 74.39
"Standard" and Cl-doped-ablator targets used during the deceleration phase experiments. The distance from the Ti-doped layer and the inner surface of the shell can be varied from 0 to 6 μm .

For future experiments the single-beam uniformity on the OMEGA laser system will be improved such that the on-target irradiation uniformity will be $<1\% \sigma_{\text{rms}}$. This will be achieved through the use of distributed phase plates (DPP's),²⁴ 2-D smoothing by spectral dispersion (2-D SSD),²⁵ and distributed polarization rotators (DPR's).²⁶ However, current uniformity levels using unsmoothed beams are predicted to be in the region of 20% or more. To predict the effect these nonuniformities might have on capsule implosions, simulations were performed using the 2-D hydrodynamic code *ORCHID*. The simulations used the actual laser-beam nonuniformity spectrum, measured from single-beam, equivalent-target-plane (ETP) images mapped onto a sphere with the appropriate overlap parameters. Even modes 2 to 200 were consistent with each mode multiplied by $\sqrt{2}$ to account for the odd modes. Figure 74.40 shows predicted mass-density profiles at a time when the shell has reached half its initial radius for two cases: a 1-ns square pulse and a 1-ns FWHM Gaussian. In each case the shell is already showing signs of severe disruption, with the structure in the Gaussian case exhibiting longer-wavelength structures. For both cases the outside of the shell is more perturbed than the inside. As a check on the *ORCHID* predictions, we carried out a number of planar-target radiography experiments, using unmodulated foils of similar thickness (20 μm) and driven with similar intensities to the spherical targets. Figure 74.41 shows radiographs recorded on the x-ray framing camera for both the 1-ns square pulse and the 1-ns Gaussian, together with the predicted foil trajectories in each case. The radiographs show qualitative agreement with the *ORCHID* simulations in Fig. 74.40, both in terms of the type of structure seen and the fact that the Gaussian pulse shows longer-wavelength structure. Note that the Gaussian case is significantly more nonuniform despite having undergone less displacement. This is primarily due to the fact that the Gaussian pulse is predicted to imprint a factor of about 2.5 larger than the square pulse. The growth rates in the two cases are similar since the higher acceleration resulting from the square pulse is compensated by a higher ablation velocity. For an imploding target the growth factor will be larger for a Gaussian pulse because the shell will take longer to reach the same radial position.

Clearly implosions driven by these levels of nonuniformity are expected to be severely disrupted. For comparison purposes only, we investigated a series of targets in which the outer 6 to 7 μm of the ablator was replaced with $\text{C}_8\text{H}_7\text{Cl}$. The presence of chlorine in the ablator serves to radiatively heat the shell, causing it to decompress. The resultant reduction in peak shell density causes an increase in the ablation velocity V_a , thereby reducing the RT growth [see Eq. (1)]. (It should,

however, be pointed out that the radiation preheat in such a target does reduce the convergence ratio and 1-D performance of the implosion.) Figure 74.42 shows the *ORCHID* simulation for a target with a Cl-doped ablator. Comparison with Fig. 74.40 shows a clear improvement in the shell uniformity. This improvement is also in agreement with experimental measurements detailed in Ref. 20, in which delayed burnthrough

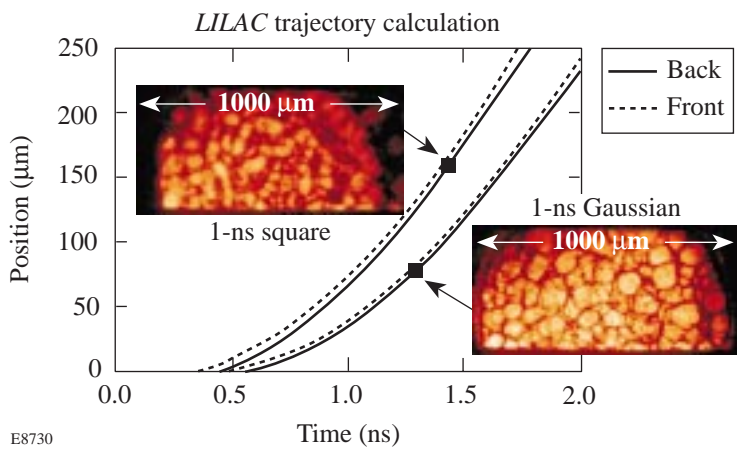
times were observed for targets with Cl-doped ablators. *ORCHID* simulations near the time of peak compression are shown in Fig. 74.43. The undoped shell in Fig. 74.43(a) shows that although the core region appears to form relatively uniformly, the shell is clearly severely disrupted. In contrast, Fig. 74.43(b) shows a shell that is still relatively intact, although still not entirely uniform.



TC4583

Figure 74.40

Shell conditions from *ORCHID* simulations compared for (a) a 1-ns square pulse and (b) a 1-ns Gaussian pulse irradiating the standard target. The actual laser beam nonuniformity measured from ETP images was used. The contours are for the mass density.



E8730

Figure 74.41

Backlit images from an experiment in which five unsmoothed OMEGA beams were focused on a planar 20-μm CH target confirm qualitatively the *ORCHID* simulation results in Fig. 74.40. The zero time for the Gaussian pulse is at 10% of peak intensity.

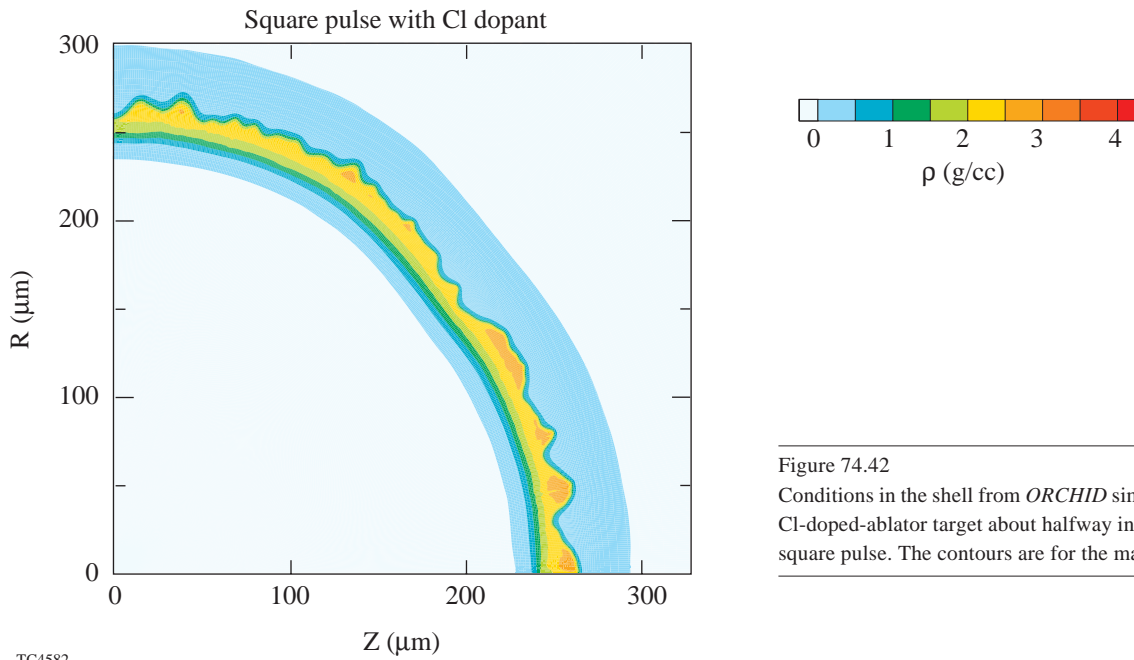
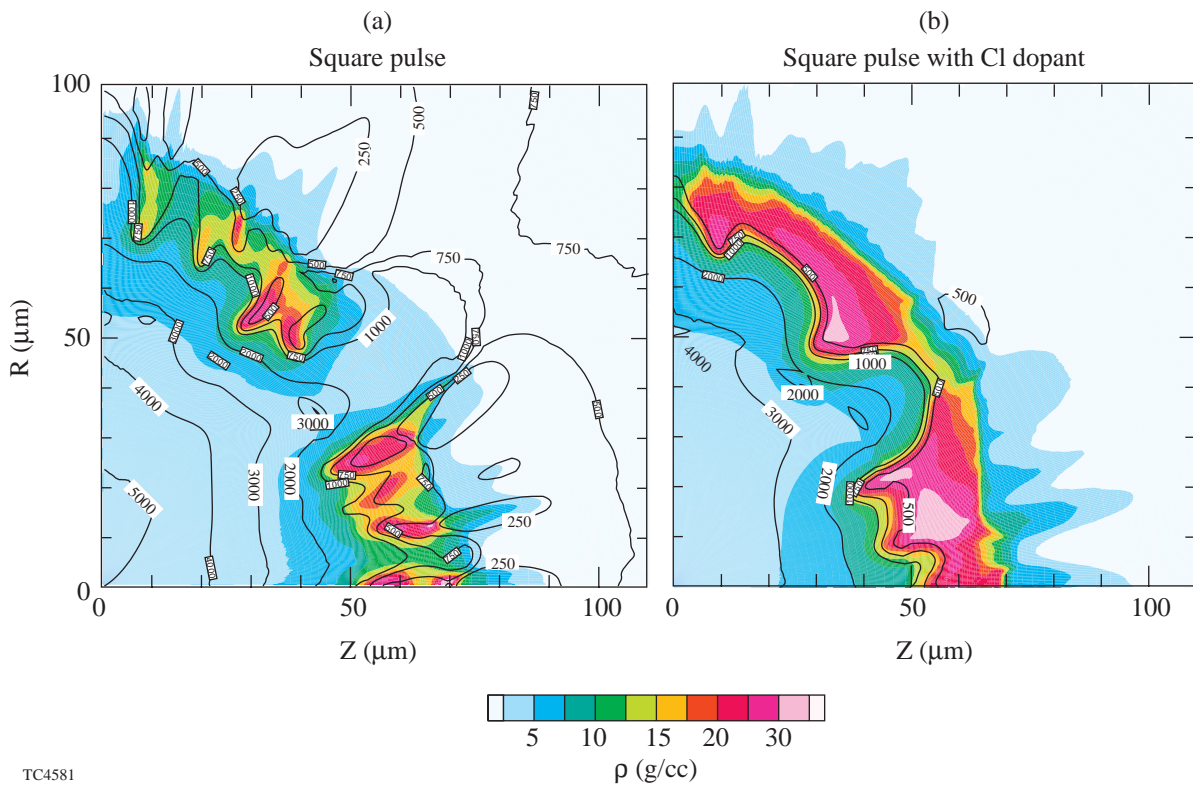


Figure 74.42
Conditions in the shell from *ORCHID* simulations compared for the Cl-doped-ablator target about halfway into the implosion for a 1-ns square pulse. The contours are for the mass density.

TC4582



TC4581

Figure 74.43
Core conditions from *ORCHID* simulations compared for (a) the standard target and (b) the Cl-doped target near time of peak core density for a 1-ns square pulse. The filled contour areas denote the mass density levels and the contour lines denote the electron temperature levels.

The experimental implosions were analyzed using a large number of diagnostics. Time-resolved imaging of the later stages of the shell trajectory and the core formation was recorded using a gated x-ray pinhole camera,^{27,28} filtered to record emission >2 keV. Figure 74.44 shows a comparison of the measured shell and core radii as a function of time, compared with 1-D *LILAC* simulations. This comparison demonstrates our ability to reproduce the zeroth-order hydrodynamics of the implosion. Time-resolved x-ray spectra from the targets were recorded using a pair of streaked spectrographs. Both instruments used a RbAP crystal to disperse the spectrum onto a 250-Å Au photocathode. One spectrometer was set up with a wavelength range of ~ 2.8 to 4.3 Å to cover the Ar *K*-shell emission from the core, with the other spectrometer covering Ti and Ar emission in the approximate range of 1.9 Å to 3.4 Å. In each case the spectral resolution was approximately $E/\Delta E \sim 500$. Temporal resolution was 20 to 30 ps, depending on the camera used. The data were recorded on Kodak T-max 3200 film, digitized using a PDS microdensitometer and then corrected for film sensitivity and streak-camera-induced temporal curvature.²⁹ The sweep speed of each streak camera was measured using a temporally modulated fiducial pulse, although no absolute timing reference was used during actual target shots. The spectrometer dispersion was calculated using published wavelengths for the Ar and Ti lines.

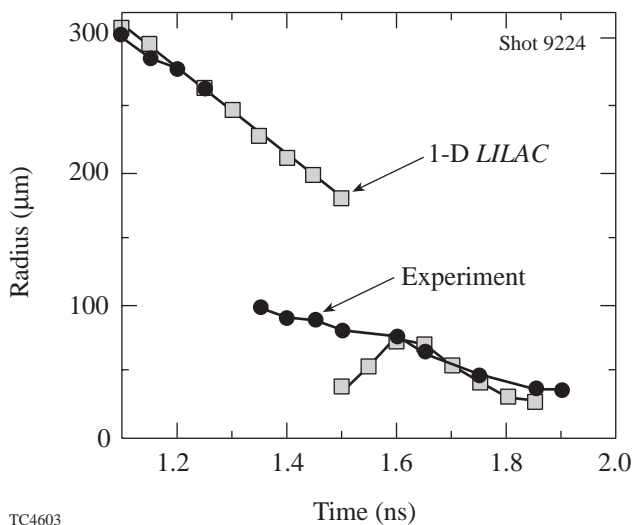


Figure 74.44

Trajectories of the peak emission from the framing camera images and from simulated images. The jump in the middle of the trajectories occurs when the peak emission moves from the heat front to the core.

Figure 74.45 shows a pair of time-resolved x-ray spectra recorded from the doped target implosions, one from a target with the Ti-doped layer at the gas/shell interface and the other with the Ti-doped layer situated 4 μm from the interface. In both streaks, Ar line emission, resulting from the initial shock heating of the core gas, appears first, followed by continuum emission from the stagnation. In Fig. 74.45(a), Ti He-like and H-like line emission from the inside surface of the shell can be seen a short time after the Ar emission, whereas the Ti in the buried layer is observed only in absorption. This absence of line emission occurred even when the Ti-doped layer was as close as 0.5 μm from the interface. Targets with a Cl-doped ablator showed little or no Ti emission, regardless of the position of the layer, in agreement with *LILAC* predictions.

The absorption feature seen in Fig. 74.45(b) around 4.6 keV corresponds to unresolved transitions of the type $1s-2p$ in titanium ions with incomplete *L* shells: Ti^{+13} to Ti^{+20} , formed when continuum from the core traverses the cold titanium layer. The envelope of the absorption feature, which changes as a function of time, indicates the ion specie of maximum abundance. The amount of absorption depends primarily on the areal density of the absorption region, but also on its temperature T and density ρ . It has been shown, however, that the measured integral over the absorption feature, together with the knowledge of the ion of peak absorption (which also depends on both T and ρ) can yield the areal density to within $\pm 25\%$ without knowing the temperature or the density.^{30,31} Typical data is plotted in Fig. 74.46, together with the $\rho\Delta R$ predicted by *LILAC* for both a CH and a Cl-doped ablator. The measured areal density for the “standard” capsule case approximately follows the continuum emission and falls well below the *LILAC* prediction. This is not entirely surprising, based on the shell disruptions seen in Fig. 74.43(a). It is also possible that for such a severely distorted shell, low-density “holes” in the shell will cause the inferred areal density to be underestimated because the unabsorbed background signal distorts the spectrum. In contrast, the $\rho\Delta R$ measurements in Fig. 74.46(b) approach more closely to the 1-D simulations. In this shot, the timing of the density peak, delayed relative to the continuum emission, shows one of the limitations to this method since in the absence of any continuum emission we are unable to measure the $\rho\Delta R$ by absorption methods.

Measurements of the core/hot-spot region were carried out using both neutron-based and x-ray spectroscopic measurements. The burn history of these capsules was measured using the neutron temporal diagnostic (NTD).^{32,33} Neutron collisions with a BC-422 plastic scintillator convert neutron kinetic

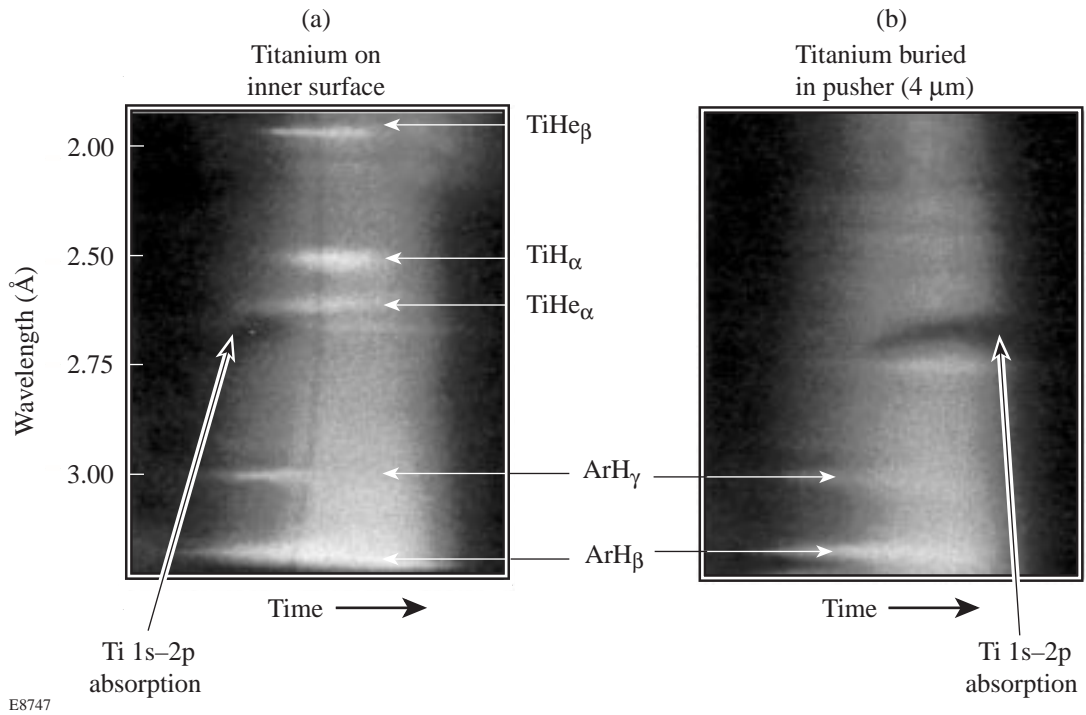


Figure 74.45
Time-resolved spectra for two positions of the Ti-doped layer for a standard target and a 1-ns square pulse:
(a) at the inner surface and (b) $4 \mu\text{m}$ from the inner surface.

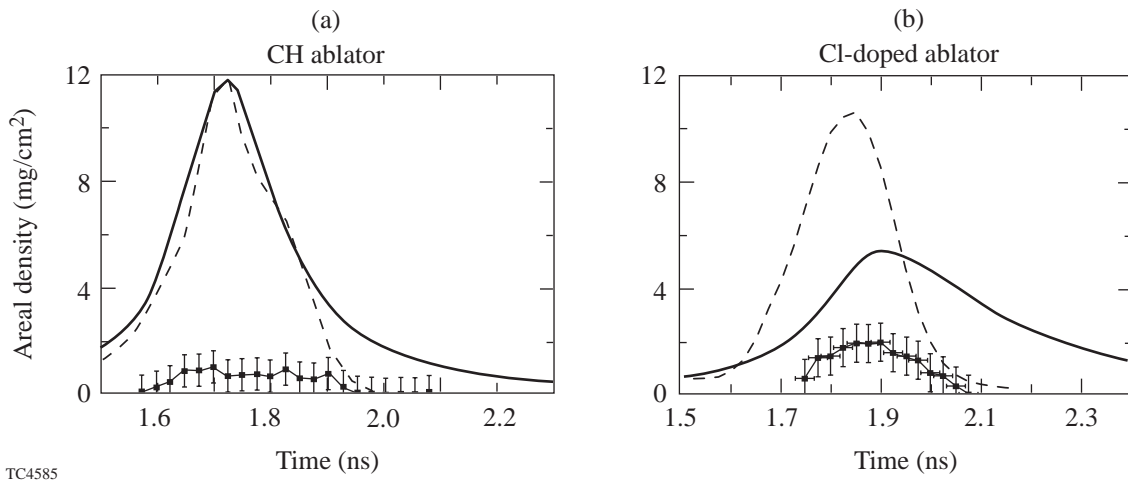


Figure 74.46
Areal densities obtained from the Ti absorption band (curve with error bars) and from the 1-D *LILAC* simulation (solid line) as a function of time for (a) the standard target and (b) the Cl-doped-ablator target. In both cases the Ti-doped layer was $4 \mu\text{m}$ from the inner surface. Also shown is the integrated continuum emission (dashed line) from the measured spectrum. Timing was made by matching the measured and predicted continuum peaks. The areal density can be measured only when the core emits continuum radiation.

energy to 350- to 450-nm-wavelength light, which is relayed to the photocathode of a fast streak camera whose output image is recorded by a charge-coupled device (CCD) camera. The temporal distribution of the emitted light is the convolution of the neutron emission history with the scintillator response; thus, the burn history is encoded in the leading edge of the light pulse. (The streak camera also records an optical fiducial signal to provide an absolute time base.) The shape of the neutron temporal distribution is obtained by deconvolving the effect of the scintillator decay rate from the recorded neutron signal. The quality of each deconvolution is checked by comparing the recorded signal with the convolution of the burn history and the exponential decay of the scintillator. Streak camera flat-field and time-base corrections are included in the signal processing. On OMEGA, NTD has demonstrated sensitivity to DD neutrons at yields above 1×10^8 and a temporal resolution of 25 ps. Figure 74.47(a) shows the measured neutron-production rate for a shot with a CH ablator, together with the rate predicted by *LILAC*. The rates agree fairly well early in time, when neutron production is dominated by the initial shock heating and compression, but as the implosion progresses toward full stagnation, where neutrons will be produced mainly by compression heating of the core, the measured rate falls significantly short of the 1-D predictions by a factor of about 20 to 30. We are, however, able to see a significant difference for implosions with the Cl-doped ablator [Fig. 74.47(b)]. In this case the predicted yield is lower due to radiative losses and preheating of the core. The measured neutron-production rates, however, come much closer to the

simulations (a factor of 4 to 5 at peak production), although the experimental yield still cuts off earlier than the simulations.

Additional measurements of conditions inside the core were carried out by spectroscopic analysis of the *K*-shell line emission from the argon dopant.^{34,35} For temperature and density regimes typically found in these implosions close to stagnation, the line shapes emitted by the *K*-shell argon ions depend strongly on electron density, while remaining relatively insensitive to changes in temperature. This fact combined with the temperature and density dependence of the relative intensity of the *K*-shell lines and their associated *L*-shell satellites allows the use of the argon line spectrum as an indicator of electron density and temperature. The effects of opacity broadening on the utility of this diagnostic are mitigated by the small concentration of argon in the fuel.

Stark-broadened line profiles for the argon He- γ , He- δ , and Ly- β resonant transitions and associated Li-like satellites were calculated using a second-order quantum mechanical relaxation theory.^{36,37} These line profiles were combined using relative intensities derived from a detailed non-LTE kinetics code³⁸ corrected for the effects of radiative transfer using an escape-factor approximation.³⁹ The final state populations of the lines in the model were also derived from the results of the kinetics code. Source size was derived by assuming the emission was that of a homogeneous spherical region whose size was determined consistently with the electron number density. The Stark-broadened line profiles were cor-

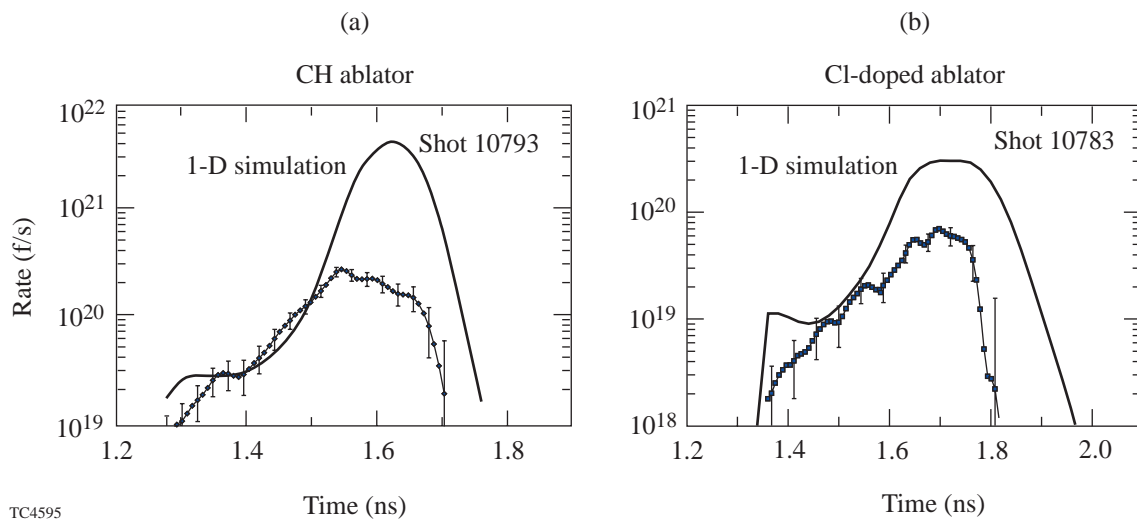


Figure 74.47

Neutron production rate obtained from the neutron temporal diagnostics (NTD) (curve with error bars) and from 1-D *LILAC* simulations (solid line) for (a) the standard target and (b) the Cl-doped-ablator target.

rected for the effects of opacity using a slab opacity model.⁴⁰ A similar theoretical spectrum was used in the analysis of the argon He- β line and its associated lithium-like satellites in Ref. 35. An example of the fits for shot 10778 is shown in Fig. 74.48. Comparison of the theoretical spectrum, after convolution with an appropriate instrumental response function, with time-resolved experimental spectra leads to an inference of the emissivity-averaged plasma electron temperature and density. Differences between the best-fitting theoretical spectrum and the experimental spectrum indicate the possible existence of gradients in the strongly emitting region of the plasma.

Figure 74.49 shows inferred electron temperature and density measurements as a function of time for the CH ablator target, imploded with the 1-ns square pulse. The temperatures and densities agree fairly well with the 1-D *LILAC* predictions at early times, but as the stagnation progresses, both parameters fall well short of the ideal case. These results are in qualitative agreement with the fusion-rate measurements. For the Cl-doped ablator (Fig. 74.50), the agreement between experiment and 1-D simulation is much closer, although the temperature still reaches only 75% of predicted.

Discussion and Conclusion

We have presented results that are part of an integrated program to investigate the physics of direct-drive ICF capsule implosions. Imprint and RT growth have been investigated in planar geometry using radiography of accelerated foils. The

growth rates measured for CH foils are in excellent agreement with hydrocode simulations. The physics of the deceleration phase has been studied using a series of doped surrogate capsules. The main goal of these experiments was to develop techniques to diagnose the conditions in the shell (main fuel layer) and in the core (hot spot). The shell has been diagnosed using time-resolved spectroscopy of a Ti-doped tracer layer. With unsmoothed beams, experiments and simulations indicate that the shell is severely disrupted at time of shock convergence. When a Cl-doped ablator was used, the $\rho\Delta R$ inferred from the Ti absorption feature was much closer to 1-D predictions, confirming our diagnostic sensitivities to changes in target performance. These observations support the *ORCHID* simulations, which predict that the addition of a Cl-doped ablator results in a more intact shell.

The core has been diagnosed by both time-resolved neutron diagnostics and time-resolved spectroscopy of the Ar fuel dopant. From the analysis of the Ar line emission we find that the core conditions (electron densities and temperatures) just after the shock has reached the target center are close to those predicted by 1-D *LILAC* simulations. The same conclusion is reached from the analysis of the neutron-production rate. These conclusions are in qualitative agreement with *ORCHID* simulations, which predict near-spherical temperature profiles in the core. Conditions in the core deteriorate during compression and stagnation: both the electron temperature and density fail to reach *LILAC* predictions. This deterioration in core conditions occurs for both the square pulse and the Gaussian

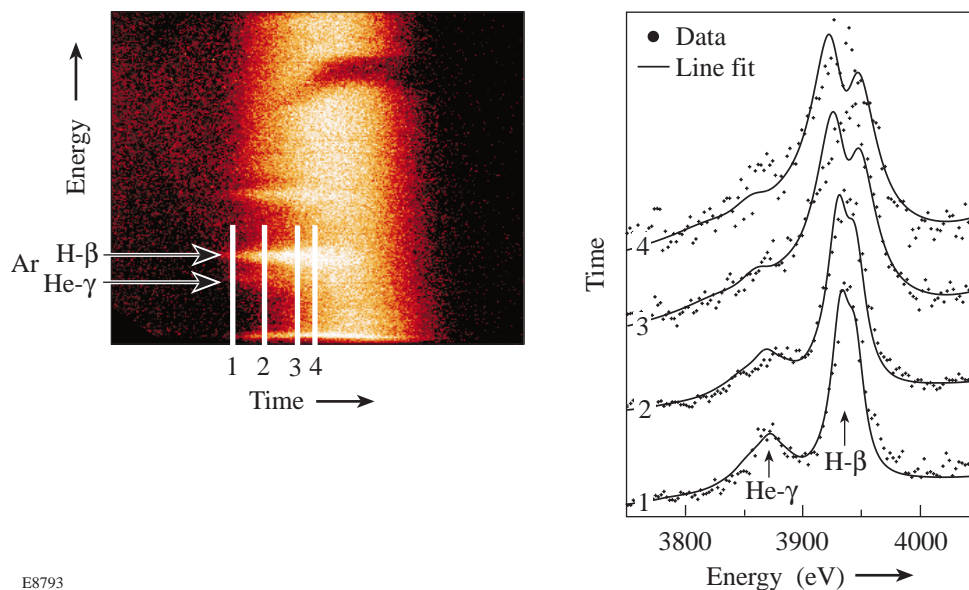


Figure 74.48
Time-resolved experimental spectrum and lineouts of the Ar H- β and He- γ lines for four times. The dots are the experimental values, and the lines are best fits from a quantum theory model combined with a non-LTE kinetics code^{36–39} for a given electron temperature and density.

E8793

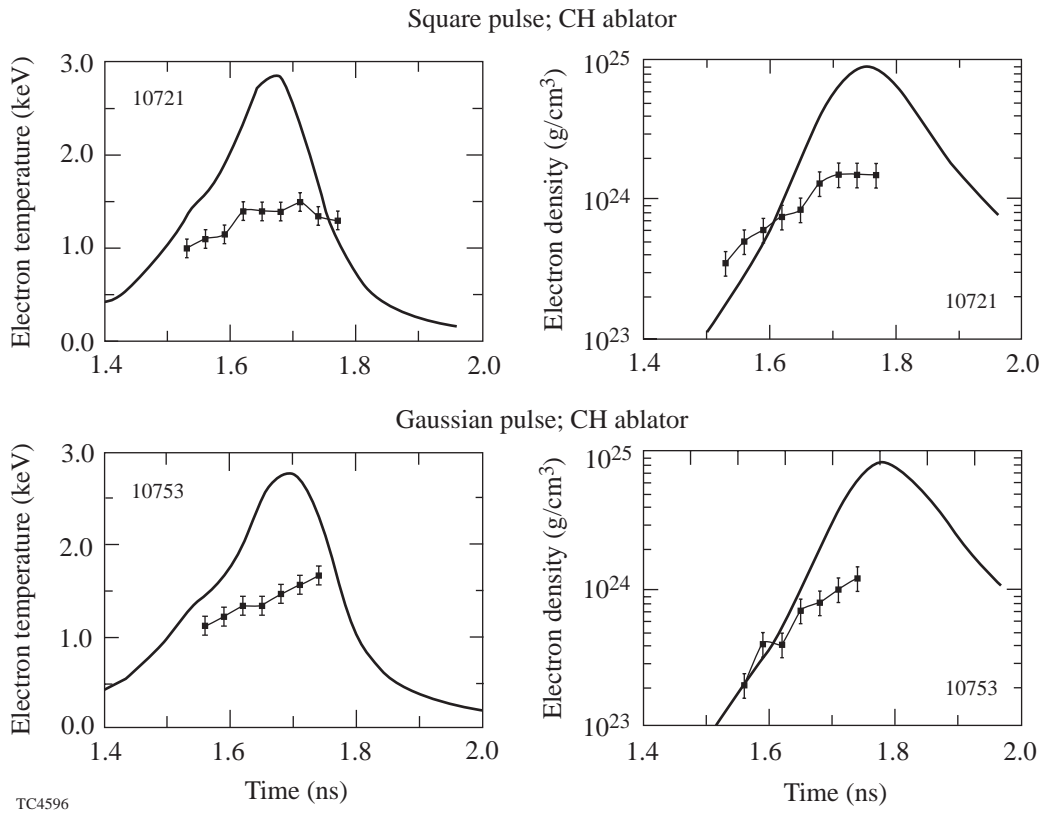


Figure 74.49 Measured and predicted electron temperatures and densities for the standard target for 1-ns square and Gaussian pulses. The predicted temperatures are mass-averaged temperatures from 1-D *LILAC* simulations (solid line).

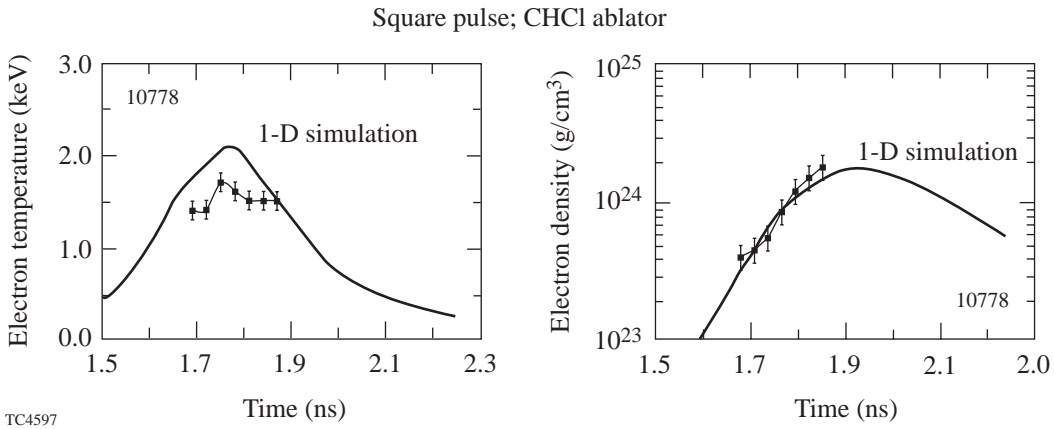


Figure 74.50 Measured and predicted electron temperatures and densities for the standard target and a Cl-doped-ablator target for a square pulse. The predicted temperatures are mass-averaged temperatures from 1-D *LILAC* simulations (solid line).

pulse. These observations indicate that final compression and resulting PdV work are not effective because the shell is probably not integral. Both diagnostics—time-resolved spectroscopy and neutron time detector—showed results that were closer to 1-D predictions when a Cl-doped ablator was used in agreement with simulations that predict reduced RT growth for those targets. The agreement between neutron and x-ray diagnostics is encouraging since cryogenic targets will be diagnosed primarily by neutron and charged-particle methods.

In conclusion, we have carried out initial mix implosion experiments with the unsmoothed OMEGA laser system to establish a base-line database for comparison with upcoming experiments in which full beam smoothing will have been implemented. We have also ascertained that the set of diagnostics used in these experiments can measure shell and core conditions and will enable us to study the effect of the RT instability on the main fuel layer (shell) and hot spot (core) in cryogenic targets.

ACKNOWLEDGMENT

This work was supported by the U.S. Department of Energy Office (DOE) of Inertial Confinement Fusion under Cooperative Agreement No. DE-FC03-92SF19460, the University of Rochester, and the New York State Energy Research and Development Authority. The support of DOE does not constitute an endorsement by DOE of the views expressed in this article.

REFERENCES

1. T. R. Boehly, D. L. Brown, R. S. Craxton, R. L. Keck, J. P. Knauer, J. H. Kelly, T. J. Kessler, S. A. Kumpan, S. J. Loucks, S. A. Letzring, F. J. Marshall, R. L. McCrory, S. F. B. Morse, W. Seka, J. M. Soures, and C. P. Verdon, *Opt. Commun.* **133**, 495 (1997).
2. Lord Rayleigh, *Proc. London Math. Soc.* **14**, 170 (1883); G. Taylor, *Proc. R. Soc. London Ser. A* **201**, 192 (1950).
3. R. D. Richtmyer, *Commun. Pure. Appl. Math.* **XIII**, 297 (1960); E. E. Meshkov, *Izv. Akad. Nauk. SSSR Mekh. Zhidk. Gaza* **4**, 33 (1970).
4. H. Takabe *et al.*, *Phys. Fluids* **28**, 3676 (1985).
5. R. Betti, V. N. Goncharov, R. L. McCrory, P. Sorotokin, and C. P. Verdon, *Phys. Plasmas* **3**, 2122 (1996).
6. O. L. Landen *et al.*, *J. Quant. Spectrosc. Radiat. Transfer* **54**, 245 (1995).
7. C. J. Keane *et al.*, *J. Quant. Spectrosc. Radiat. Transfer* **54**, 207 (1995).
8. O. L. Landen *et al.*, *Phys. Plasmas* **3**, 2094 (1996).
9. M. C. Richardson, P. W. McKenty, F. J. Marshall, C. P. Verdon, J. M. Soures, R. L. McCrory, O. Barnouin, R. S. Craxton, J. Delettrez, R. J. Hutchison, P. A. Jaanimagi, R. Keck, T. Kessler, H. Kim, S. A. Letzring, D. M. Roback, W. Seka, S. Skupsky, B. Yaakobi, S. M. Lane, and S. Prussin, in *Laser Interaction and Related Plasma Phenomena*, edited by H. Hora and G. H. Miley (Plenum Press, New York, 1986), Vol. 7, pp. 421–448.
10. B. I. Bennett *et al.*, Los Alamos National Laboratory Report LA-7130 (1978). Copies may be obtained from the National Technical Information Service, Springfield, VA 22161.
11. R. L. McCrory and C. P. Verdon, in *Inertial Confinement Fusion*, edited by A. Caruso and E. Sindoni (Editrice Compositori, Bologna, Italy, 1989), pp. 83–124.
12. D. H. Kalantar, M. H. Key, L. B. Da Silva, S. G. Glendinning, B. A. Remington, J. E. Rothenberg, F. Weber, S. V. Weber, E. Wolftrum, N. S. Kim, D. Neely, J. Zhang, J. S. Wark, A. Demir, J. Lin, R. Smith, G. J. Tallents, C. L. S. Lewis, A. MacPhee, J. Warwick, and J. P. Knauer, *Phys. Plasmas* **4**, 1985 (1997).
13. C. J. Pawley *et al.*, *Phys. Plasmas* **4**, 1969 (1997).
14. S. G. Glendinning, S. N. Dixit, B. A. Hammel, D. H. Kalantar, M. H. Key, J. D. Kilkenny, J. P. Knauer, D. M. Pennington, B. A. Remington, R. J. Wallace, and S. V. Weber, *Phys. Rev. E* **54**, 4473 (1996).
15. H. Azechi *et al.*, *Phys. Plasmas* **4**, 4079 (1997).
16. R. J. Taylor *et al.*, *Phys. Rev. Lett.* **76**, 1643 (1996).
17. T. R. Boehly, V. A. Smalyuk, D. D. Meyerhofer, J. P. Knauer, D. K. Bradley, C. P. Verdon, and D. Kalantar, in *Laser Interaction and Related Plasma Phenomena*, edited by G. H. Miley and E. M. Campbell (American Institute of Physics, Woodbury, NY, 1997), Vol. 406, pp. 122–129.
18. B. A. Remington *et al.*, *Phys. Fluids B* **4**, 967 (1992).
19. J. P. Knauer, C. P. Verdon, D. D. Meyerhofer, T. R. Boehly, D. K. Bradley, V. A. Smalyuk, D. Ofer, P. W. McKenty, S. G. Glendinning, D. H. Kalantar, R. G. Watt, P. L. Gobby, O. Willi, and R. J. Taylor, in *Laser Interaction and Related Plasma Phenomena*, edited by G. H. Miley and E. M. Campbell (American Institute of Physics, Woodbury, NY, 1997), Vol. 406, pp. 284–293.
20. J. Delettrez, D. K. Bradley, and C. P. Verdon, *Phys. Plasmas* **1**, 2342 (1994).
21. D. K. Bradley, J. A. Delettrez, and C. P. Verdon, *Phys. Rev. Lett.* **68**, 2774 (1992).
22. D. K. Bradley, T. Boehly, D. L. Brown, J. Delettrez, W. Seka, and D. Smith, in *Laser Interaction and Related Plasma Phenomena*, edited by H. Hora and G. Miley (Plenum Press, New York, 1991), Vol. 9, pp. 323–334.
23. S. W. Haan, *Phys. Rev. A* **39**, 5812 (1989).
24. Y. Lin, T. J. Kessler, and G. N. Lawrence, *Opt. Lett.* **20**, 764 (1995); Laboratory for Laser Energetics LLE Review **65**, 1, NTIS document No. DOE/SF/19460-117 (1995). Copies may be obtained from the National Technical Information Service, Springfield, VA 22161.
25. S. Skupsky, R. W. Short, T. Kessler, R. S. Craxton, S. Letzring, and J. M. Soures, *J. Appl. Phys.* **66**, 3456 (1989).

26. Laboratory for Laser Energetics LLE Review **45**, 1, NTIS document No. DOE/DP40200-149 (1990). Copies may be obtained from the National Technical Information Service, Springfield, VA 22161.
27. O. L. Landen, P. M. Bell, J. A. Oertel, J. J. Satariano, and D. K. Bradley, in *Ultra-high- and High-Speed Photography, Videography, and Photonics '93*, edited by P. W. Roehrenbeck (SPIE, Bellingham, WA, 1993), Vol. 2002, pp. 2–13.
28. D. K. Bradley, P. M. Bell, J. D. Kilkenny, R. Hanks, O. Landen, P. A. Jaanimagi, P. W. McKenty, and C. P. Verdon, *Rev. Sci. Instrum.* **63**, 4813 (1992).
29. D. H. Kalantar *et al.*, in the *22nd International Congress on High-Speed Photography and Photonics*, edited by D. L. Paisley, and A. M. Frank (SPIE, Bellingham, WA, 1997), Vol. 2869, pp. 680–685.
30. B. Yaakobi, R. S. Craxton, R. Epstein, and Q. Su, *J. Quant. Spectrosc. Radiat. Transfer* **58**, 75 (1997).
31. B. Yaakobi, F. J. Marshall, D. K. Bradley, J. A. Delettrez, R. S. Craxton, and R. Epstein, *Phys. Plasmas* **4**, 3021 (1997).
32. R. A. Lerche, D. W. Phillion, and G. L. Tietbohl, in *Ultra-high- and High-Speed Photography, Videography, and Photonics '93*, edited by P. W. Roehrenbeck (SPIE, Bellingham, WA, 1993), Vol. 2002, pp. 153–161.
33. T. J. Murphy and R. A. Lerche, *ICF Quarterly Report* **3**, 35, Lawrence Livermore National Laboratory, Livermore, CA, UCRL-LR-105821-93-1 (1992). Copies may be obtained from the National Technical Information Service, Springfield, VA 22161.
34. H. R. Griem, *Phys. Fluids B* **4**, 2346 (1992).
35. D. A. Haynes, Jr., D. T. Garber, C. F. Hooper, Jr., R. C. Mancini, Y. T. Lee, D. K. Bradley, J. Delettrez, R. Epstein, and P. A. Jaanimagi, *Phys. Rev. E* **53**, 1042 (1996).
36. R. C. Mancini *et al.*, *Comput. Phys. Commun.* **63**, 314 (1991).
37. L. A. Woltz and C. F. Hooper, Jr., *Phys. Rev. A* **38**, 4766 (1988).
38. Y. T. Lee, *J. Quant. Spectrosc. Radiat. Transf.* **38**, 131 (1987).
39. R. C. Mancini, R. F. Joyce, and C. F. Hooper, Jr., *J. Phys. B: At. Mol. Phys* **20**, 2975 (1987).
40. N. D. Delamater *et al.*, *Phys. Rev. A* **31**, 2460 (1985).